




Three-dimensional measurements of an inclined vortex ring interacting with a density stratification

Johan Pinaud , Julie Albagnac *, Sébastien Cazin, Zeinab Rida,
Dominique Anne-Archard, and Pierre Brancher 

*Institut de Mécanique des Fluides de Toulouse (IMFT), Université de Toulouse, CNRS,
31400 Toulouse, France*



(Received 10 July 2020; accepted 23 September 2021; published 19 October 2021)

Vortex rings are generated every time an impulsive jet occurs in an ambient homogeneous fluid, for instance in thermal or density plumes in environmental applications. Those vortical structures, often referenced as building blocks of turbulence, exist in a wide range of scales. The velocity field associated with these toroidal vortical structures makes them self-propagating. Such vortices are likely to carry mass and momentum along their path and are therefore good candidates for driving mixing to locations that are remote from where the ring is created. In numerous environmental applications, vortex rings interact with a density stratification due to variations of salinity and/or temperature. The path followed by a light homogeneous and axisymmetric vortex ring impinging a layer of fluid stably stratified in density with a given angle θ to the vertical, along with its dynamics and subsequent reorganization, are experimentally addressed in the present study. A three-dimensional time-resolved particle tracking velocimetry technique is set up to highlight the response of the stratified layer that is characterized by the generation of baroclinic vorticity and internal gravity waves. For the experimental parameters of the present study, the vorticity generation and reorganization, as well as the internal gravity waves in the stratified layer, are shown to remain axisymmetric for normal impacts. When the vortex ring propagation axis is not aligned with the density gradient, the expected symmetry breaking of the flow is observed. For inclined impact, the flow reorganizes in the form of a vertically flattened dipolar structure. In this case, internal gravity waves radiate away from two sources that match with the dipole cores.

DOI: [10.1103/PhysRevFluids.6.104701](https://doi.org/10.1103/PhysRevFluids.6.104701)

I. INTRODUCTION

Vortex rings are ubiquitous toroidal coherent structures observed each time an impulsive jet occurs. Consequently, vortex rings are the dominant features of many natural phenomena such as smoke rings during volcano eruptive events, plumes in the convection zone on a planetary or stellar scale [1], or wakes downstream of beating structures [2,3]. A vortex ring is made of azimuthal vorticity. If the vorticity is uniformly distributed, such a vortical structure exhibits a symmetry axis along which it propagates by a self-induced effect, transporting mass and momentum on its way. The transport properties of vortex rings have been explored in many ways: encapsulation of the functional component inside frozen vortex rings [4], jellyfish swimming by reaction [5], or, more recently, dandelion seed flight [6]. Hence, vortex rings evolving in homogeneous fluids have been studied in the minutest detail for decades [7–11] and their behavior in stratified flows is the object of recent studies (see, for instance, [12,13]). Olsthoorn and Dalziel [13] recently depicted

*julie.albagnac@imft.fr

the three-dimensional vortex-ring azimuthal instability in the presence of a stratified interface by reconstruction of the whole three-dimensional (3D) field thanks to multiple experiments.

Regarding environmental applications (oceans, atmosphere), most of the flows are stratified due to salinity and/or temperature vertical gradients. In such a background stratification, vertical perturbations of isopycnals can lead to internal gravity wave generation. Indeed, when a solid body oscillates in a density stratification, parcels of fluid that are initially laying at their vertical equilibrium position are horizontally and vertically displaced, becoming either heavier or lighter than their environment. They will subsequently oscillate for a while at a given frequency that depends on the background stratification in order to return to their equilibrium position. The stratification is characterized by the Brunt-Väisälä frequency, also called buoyancy frequency, and defined, with z positive downwards, as

$$N = \sqrt{\frac{g}{\rho} \frac{\partial \rho}{\partial z}},$$

where g is the gravity acceleration, ρ is a density of reference, and $\frac{\partial \rho}{\partial z}$ is the vertical density gradient. So-called internal gravity waves are triggered if the solid body oscillates at frequencies ω smaller than N [14]. They were described in detail for various shapes of oscillating bodies, for instance, a horizontal bar [15,16], a sphere [17], and a torus [18].

In the atmosphere, vertical oscillations of updrafts and downdrafts can trigger internal waves, often referred to as “internal gravity waves,” in a way similar to that of an oscillating solid body. This phenomenon has been experimentally studied by Ansong and Sutherland [19], who investigated a heavy plume normally impinging a linear stratification. In this case, internal waves were forced by vertical velocity fluctuations at the top of the plume. Recently, Brandt *et al.* [20] focused as well on the generation of internal waves by a heavy turbulent plume, this time impulsive. The plume descends into a linear stratification to a maximum depth and returns back up to its density equilibrium level. The authors noticed the generation of a transient internal wave field, carrying up to 10% of the initial energy associated with the forced plume. For vortex rings generated in a stratified layer and propagating quasihorizontally, Scase and Dalziel [21] described the collapse of the initial vortex ring into a pancakelike dipolar vortex structure. Prior to the collapse, internal gravity waves are measured on a large frequency spectrum, similar to that produced by a towed sphere [22]. Internal waves forced by “soft structures” were also pointed out by Dintrans *et al.* [1] in solar-type stars in which cool convection plumes formed in the surrounding mantle impinge the inner radiative (and density stratified) zone, leading to the generation of internal waves likely to transport lithium to the star cores and consequently acting on the star lifetime.

In most cases, the plumes are aligned with the density gradient. Therefore, several studies involving vortex rings launched along the vertical axis and impacting a stable stratification were undertaken in order to get a better understanding of the subsequent mixing. On the one hand, at small length scales, Linden [23] has suggested that vortex rings could represent elementary bricks of turbulence. He deduced entrainment rate laws for vortex rings generated in a homogeneous fluid and impacting a sharp density jump for several ratios of buoyant to shear forces, quantified by the Richardson number, $Ri = \frac{g}{\rho} \frac{\partial \rho / \partial z}{(\partial u / \partial z)^2}$. On the other hand, as a simplification of previously mentioned larger length scale plumelike flows, Olsthoorn and Dalziel [24] have submitted a 1D model for the statistical mixing resulting from hundreds of vortex rings impinging a two-layer stratification [25]. The mixing rate, evaluated as the conversion efficiency from kinetic to potential energy, was finally shown to be Richardson independent. Other studies rather focused on the penetration and eventual reorganization of a single vortex ring impinging a stratification. Dahm *et al.* [26] and Stock *et al.* [27] proposed a criterion based on *a priori* values of Atwood ($At = \Delta \rho / 2 \bar{\rho}$) and Richardson numbers to predict the complete, partial, or nonpenetration of a vortex ring impinging a two-layer stratification. Advaita *et al.* [12] investigated the same kind of feature for a vortex ring impinging a finite linear stratification. Instabilities of the plumelike impinging structure were revealed for deep penetrative regimes [12].

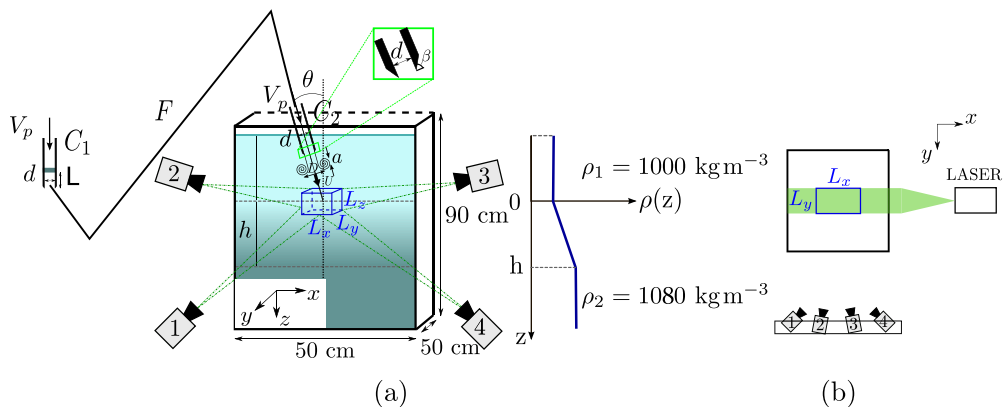


FIG. 1. Sketch (not to scale) of the experimental setup. (a) Complete view and (b) view from above.

In the present study, we investigate the behavior of a single vortex ring launched with an angle θ to the vertical and impinging a linear density stratification much thicker than the vortical structure characteristic length scale. The vortex-ring Reynolds number is kept constant and is low enough to avoid the development of azimuthal instability [7]. The Richardson number is also fixed and corresponds to a penetrative regime. Velocity measurements are performed thanks to a time-resolved 3D particle tracking velocimetry technique (4D-PTV) developed by Schanz *et al.* [28,29]. The experimental setup and the measurement technique are detailed in Sec. II. Sections III and IV give insights on the impinging vortex-ring dynamics in terms of global propagation and vorticity rearrangement, respectively. In particular, the 3D reorganization of the primary vortex-ring structure with the secondary baroclinic vorticity is examined for the *a priori* axisymmetric case associated with the normal impact. For the inclined vortex-ring impact, the expected loss of axisymmetry is revealed and the reorganization of the flow results in the generation of a pancakelike dipolar structure of which the spatial extent evolution in time is described. In Sec. V, the consequences of the impact of vortex rings in terms of internal gravity wave generation are evaluated as a function of the launch angle to the vertical. The dispersion relation of the excited waves is retrieved and shown to be that of internal gravity waves. For the inclined impact, the three-dimensional measurements reveal the loss of the cone feature of the wave pattern and the appearance of two sources, located close to the newly generated dipolar vortex cores, from where internal gravity waves radiate away. Finally, Sec. VI presents the conclusions of the present work and perspectives for future research.

II. EXPERIMENTAL SETUP AND 3D TIME-RESOLVED MEASUREMENTS

A. Experimental facility

a. Vortex-ring generator. Figure 1 shows a sketch of the experimental setup. Vortex rings are generated in a $L \times W \times H = 50 \times 50 \times 90 \text{ cm}^3$ tank thanks to a piston-cylinder system. The piston-cylinder apparatus allows control of the generation of vortex rings and has been employed in numerous studies (as an example, see [8,30,31]). In the present configuration, the piston-cylinder system is deported outside of the tank and connected with the vortex-ring cylinder by way of a flexible tube in order to easily adjust the orientation of the launcher. As sketched in the upper left part of Fig. 1(a), a cylinder C_1 (the actuating cylinder) is connected to a flexible tube F , itself connected to a rigid cylinder C_2 (the vortex ring launcher), similar to C_1 , that is immersed in the tank. The whole system ($C_1 + F + C_2$) is filled with the fluid lying in the upper part of the tank. A piston of diameter $d = 2 \text{ cm}$, which fits the inner diameter of C_1 , can move up and down into the cylinder along its symmetry axis. The piston is connected to a step motor whose motion is controlled in both position and velocity by a computer. In the present study, the motion of the piston is set to be as

close as possible to a square pulse: the piston starts at $t = 0$ s and reaches its command displacement speed V_p in a few milliseconds; then it travels with the constant velocity V_p over a specific stroke L , and stops in a few milliseconds. A single piston velocity ($V_p = 6 \text{ cm s}^{-1}$) has been used for all experiments in the present study.

In the following, z denotes the vertical descending direction and $z/d = 0$ marks the linear stratification upper boundary. Here, x and y are, respectively, the horizontal direction aligned with the laser beam and the direction orthogonal to it, such that (x, y, z) is a right-handed coordinate system. The axes origin $x/d = y/d = z/d = 0$ is aligned with the vortex-ring launcher axis, is centered on the measurement volume in both horizontal directions, and belongs to the stratification upper boundary when the tank is at rest.

As compressibility is negligible for the piston velocity considered here, when the piston pushes a volume of fluid on a stroke length L in C_1 , the same volume $L\pi d^2/4$ is ejected at the exit of C_2 . The stroke length is set to $L = 3d$ in order to generate a single vortex ring [31] and the piston motion duration can reasonably be considered equal to $t_p = 3d/V_p$. The exit of C_2 is sharpened by a bevel on the outside of the tube [angle $\beta \sim 75^\circ$, see Fig. 1(a)] to help the vortex-ring formation through the coiling of the ejected vortex sheet. Once the piston stops at $t^* = tV_p/d = 3$, the vortex ring detaches from the exit of C_2 and propagates away along its axis of symmetry by momentum conservation. The vortex-ring propagating velocity V_{VR} is proportional to V_p ($V_{VR} \approx 0.6V_p$) and its diameter D is proportional to the diameter d of C_2 ($D \simeq 1.5d$), in good agreement with previous observations [30,31].

The vortex-ring axis of propagation initially coincides with the orientation of cylinder C_2 that is set on a pivoting system and makes an angle θ relative to the vertical. Two orientations are considered in the present study: $\theta = 0^\circ$ (vertical launching) and $\theta = 30^\circ$ (large deviation to the vertical). Whatever the orientation of C_2 , the centerline of the tube exit is immersed at $5d$ below the free surface to avoid any influence of the free surface on the vortex-ring generation.

b. Density stratification. The tank is filled through its drain hole at the bottom as described hereafter. First, a light homogeneous layer of density $\rho_1 = 1000 \text{ kg m}^{-3}$ with a thickness $10d$ is inserted. Then, the double-bucket method described by Oster [32] is used to fill a stably linearly stratified layer of thickness $11d$ going from ρ_1 at its top to $\rho_2 = 1080 \text{ kg m}^{-3}$ at its bottom. A particular care was taken to fill the tank smoothly in order to minimize mixing. For this purpose, the filling is done by gravity and the injected fluid is reoriented in a horizontal plane thanks to a circular plate fixed to the bottom of the tank just above the drain hole. Finally, a homogeneous layer of density ρ_2 is gently injected underneath. At the end of the filling, as sketched in Fig. 1(a), the light layer will extend from $z/d = -10$ (free surface) to $z/d = 0$, the stratified layer will extend from $z/d = 0$ to $z/d = 11$, and the heavy homogeneous layer will extend from $z/d = 11$ to $z/d \approx 30$ (bottom of the tank). The light fluid of density ρ_1 is a mixture of salt water (80% in volume, density 1052 kg m^{-3}) and ethanol (20% in volume, density 789 kg m^{-3}) so that the optical refractive index of the fluids used for the double-bucket method are the same ($n = 1.3553$ with a maximum uncertainty of 10^{-4}). A high-precision refractive index matching is crucial in order to properly follow particles crossing isopycnals. Note that adding salt to the upper layer reduces the density difference between the fluid and seeding particles, reducing their settling velocity. The optical refractive index n is matched prior to the filling, which ensures that n is constant in the whole tank. Moreover, a viscosimeter was used to measure the dynamic viscosity of the light homogeneous layer $\mu_1 = 1.8 \times 10^{-3} \text{ Pa s}$.

Vertical density profiles were measured with a translating conductivity probe before and after each vortex-ring launch. A calibration of the conductivity probe is necessary and realized using five samples $E_{i=1\dots 5}$ made of different proportions of water, salt, and ethanol. Samples E_1 and E_5 are made up of the light fluid at ρ_1 (containing the highest concentration of ethanol) and the heavy fluid at ρ_2 (without ethanol), respectively. The three other samples were obtained by mixing solutions E_1 and E_5 in the following proportions: $E_2 = 25\%E_1 + 75\%E_5$, $E_3 = 50\%E_1 + 50\%E_5$, and $E_4 = 75\%E_1 + 25\%E_5$. The sample density was measured using a portable density meter

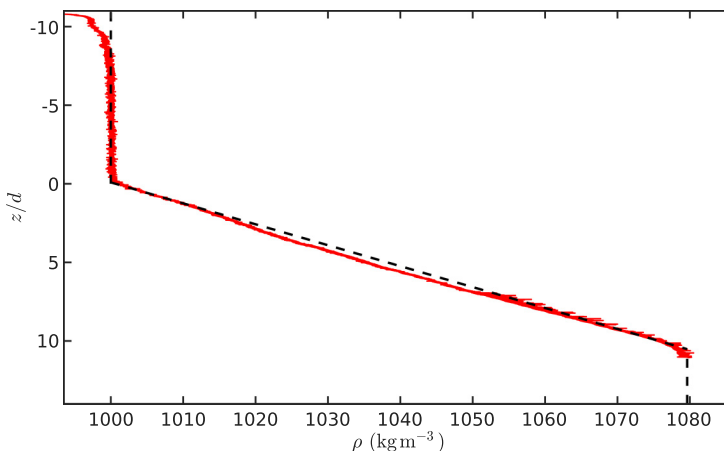


FIG. 2. Vertical density profile targeted (dashed black) and measured with the conductivity probe (red).

(DMA, Anton-Paar) with an accuracy of $\pm 0.5 \text{ kg m}^{-3}$. This uncertainty spreads to the calibration of the conductivity probe leading to a global accuracy of $\pm 2 \text{ kg m}^{-3}$.

Olsthoorn and Dalziel [25], who sent vortex rings over a density interface with orthogonal impacts, showed that hundreds of launches were necessary to significantly modify the density profile. For the present study, an example of such a density profile measured with the conductivity probe after a single vortex-ring launch is shown in Fig. 2 and, indeed, no alteration of the stratification was measurable. These measurements are useful to properly define the upper boundary of the linear stratification $z/d = 0$ and the density gradient in the linearly stratified zone. The buoyancy frequency, associated with the linearly stratified layer and defined as $N = \sqrt{\frac{g}{\rho_1} \frac{\Delta\rho}{h}}$, with g the gravity acceleration, $\Delta\rho = \rho_2 - \rho_1$, and h the stratified layer thickness, is computed from the density profiles and is kept constant at $N = 1.88 \text{ rad s}^{-1}$. Furthermore, note that the vortex rings generated in the present study are small and weak enough so that the linearly stratified layer is seen as an infinite one during the propagation of the rings.

B. 4D-PTV technique and validation

For the 3D measurements, the commercial code DaVis, developed by LaVision, was used. Nevertheless, it is necessary to be meticulous on numerous points to ensure the reliability of the measurements and the obtained results. The objective here is to present the various points of vigilance and validation of the calculation implementation.

a. Calibration of the setup (part 1) with a calibration plate. For the 4D-PTV technique, 3D trajectories of seeding particles are tracked by four cameras. The calibration allowing the volumetric reconstruction is of major importance and each step of this process is described hereafter.

First, the tank is filled with a homogeneous fluid with an optical refractive index $n = 1.3553$, equal to that of the final stratified tank. Then, as sketched in Figs. 3(a) and 3(b), a biplanar calibration target from LaVision (Ref. No. 309-15-SSDP) is immersed in the tank alongside the tank front face. The calibration target, homogeneously illuminated with a white light and imaged by the four cameras, is moved along the y axis, stopping at seven positions spaced 25 mm apart from -75 to $+75$ mm. From this first calibration step, DaVis creates a transfer function (TF) of the setup [33], also referred to as a mapping function, that allows the reconstruction of the particle 3D position from the four frames taken by the four cameras. After this first calibration step, the tank is emptied and refilled with the desired density stratification.

b. Seeding and imaging. The tracers used in the present study are fluorescent red polyethylene microspheres (Cospheric) with diameter 53–63 μm and density $\rho_p = 1050 \text{ kg m}^{-3}$. Once the tank

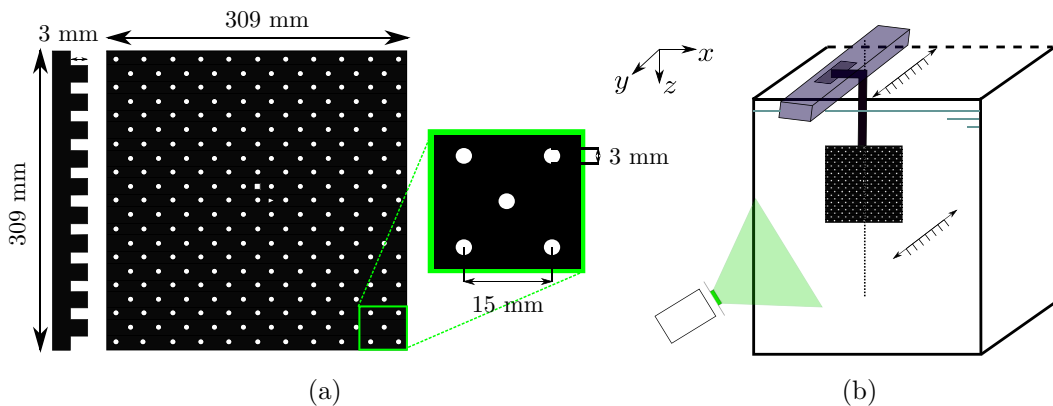


FIG. 3. Sketches of the (a) 3D biplanar calibration target and (b) calibration setup. Figures are not to scale.

is filled with the density stratification, tracers are released in the top light homogeneous layer, where their settling velocity is maximum and estimated based on the Stokes law to be about $50 \mu\text{m s}^{-1}$ (equivalently, 0.08% of the piston velocity). After about two hours, tracers are seeding the linear stratification. In addition, tracers are regularly added in the top light homogeneous part of the tank in order to maintain an adequate amount of tracers in the volume of interest.

Particles are illuminated by a 527 nm, 60 mJ double-pulsed laser (Photonics, Ref. No. Dm60-527-DH). A volume illumination optics from LaVision is used to generate an expanded and collimated laser beam with dimensions $L_x \times L_y \times L_z = 25 \times 10 \times 15 \text{ cm}^3$ (see Fig. 1). Four high-speed VEO640 Phantom cameras (Vision Research) with a full resolution of 2560×1600 pixels are synchronized and record sequences of 4D-PTV images at an acquisition frequency $f_a = 150 \text{ Hz}$. The four cameras have embedded memory (72 GB each) and can record more than 12 000 images each.

The two top cameras, numbered 2 and 3 in Fig. 1(a), are tilted 20° downwards and the two bottom ones are tilted 20° upwards. All of them are fitted with two-axis Scheimpflug mounts to deal with the oblique viewing setup and to reach the expected depth of focus. The camera support is standing alongside the tank front face and the optical distance between each camera and the tank is 140 cm. In order to minimize external optical noise, each camera lens (Zeiss 100 mm, f-number 8) is equipped with an optical high-pass filter at 540 nm so that only the fluorescent response of the seeding is received.

c. Calibration of the setup (part 2) with the seeding. The outcome of the first calibration step, with the translating target, is a mapping function from the particle position (x, y, z) , i.e., the so-called world position in Wieneke [34], to pixel coordinates in the raw image of camera i : $(x_i, y_i) = M_i(x, y, z)$. This mapping function is not perfect due to uncertainties on the plate displacement, on the pattern positions, and on potential remaining optical distortions. Moreover, the global optical setup changes slightly for various reasons (vibrations, thermal expansions, etc.) and, especially, in the present case, during the draining of the homogeneous calibration tank and the filling of the final stratification. A second calibration step, called volume self-calibration, implemented in the DaVis software and based on the work of Wieneke [34], is therefore necessary. The volume self-calibration corrects the first mapping function performed in the homogeneous tank by using information of real particle seeding in the final stratified configuration.

In practice, the stratified tank is seeded with particles and, in order to record images with different particle localizations, a weak flow is generated using a small grid gently towed in the top homogeneous light layer. Several disparity maps from one-hundred noncorrelated recordings are summed for better statistics [34] in order to correct the mapping function. Figure 4(a) shows an example of displacements corresponding to the disparity, or mismatch, between particle positions measured directly in the raw image and the ones obtained by projection of the triangulation process

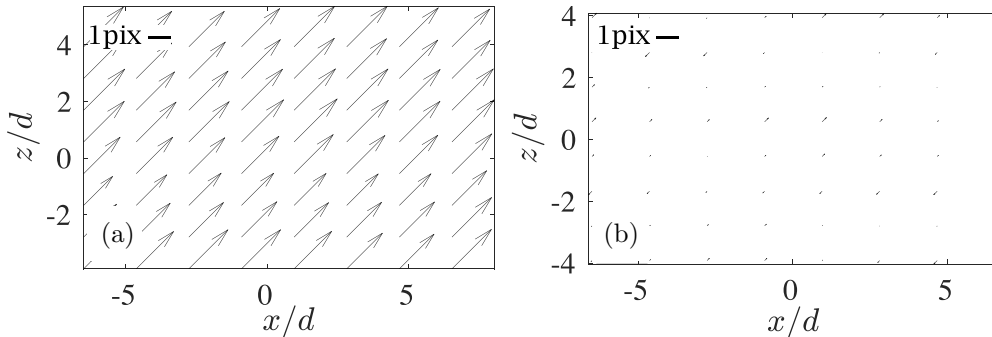


FIG. 4. Example of disparity maps obtained on one of the four cameras (a) prior to the self-calibration step, with a mean magnitude of 1.88 pixels, and (b) after the mapping function correction, with a mean magnitude of 0.08 pixels.

based on the first mapping function. Here, displacements are oriented in the same direction and reveal a mean movement of the considered camera from the bottom left corner towards the top right one with a mean magnitude of 1.88 pixels. A new mapping function based on the previous one and corrected from the disparity map is calculated and the process is iterated until displacements are lower than 0.1 pixel for all components. Once this process has converged, an optical transfer function (OTF) is generated [33]. This OTF takes into account the shape of groups of particles in subvolumes seen by each camera and is useful for the Lagrangian tracking as, among others, it facilitates the recognition of particles in consecutive frames.

d. Trajectory computation with the Shake The Box algorithm. Images are acquired using DaVis 8.4.0 software and processed using the state-of-the-art Shake The Box (STB) algorithm developed by Schanz *et al.* [33] and implemented in the commercial software of LaVision.

During an initialization phase, particles are identified using an iterative triangulation method in n_{init} consecutive frames. Only the particles found in the whole n_{init} frames are considered for trajectory computation. Here, $n_{\text{init}} = 4$ and, consequently, there are always at least four consecutive tracked positions for each particle trajectory. Then, the algorithm takes the benefit from the gained tracks to predict particle positions on the next time steps.

The use of the trajectory history to predict the next position of a particle makes the computation very efficient in terms of speed and precision. Hence, the STB algorithm can work with highly seeded flows and track hundreds of thousands of particles per time step. Schanz *et al.* [29] showed that the number of particles per pixel (ppp) does not affect the quality of the Lagrangian tracking and the STB algorithm works well up to 0.125 ppp, even if 0.05 ppp is a more standard density. In our case, the salt water and ethanol solution is not perfectly transparent and a slight turbidity is detectable when the mixture is illuminated with a laser. This limits the usable particle concentration, which ranges from 0.002 to 0.007 ppp.

e. Projection of the Lagrangian data on a Eulerian grid. A projection of the Lagrangian data on a Eulerian grid is realized using the “convert to grid” function from DaVis. The volume is divided in cubic subvolumes of 104 voxels per side with an overlap of 75%. At each time step, if there are at least three particles inside a subvolume, the average velocity is computed and gives a Eulerian velocity vector for this subvolume. By the end, Eulerian velocity fields are obtained on a grid with cubic meshes of 26 voxels per side or, equivalently, 3.1 mm per side. This projection is particularly useful to obtain Eulerian quantities, such as vorticity that is computed using a simple central finite-differencing scheme and is of great interest for our study. In the following, both Lagrangian and Eulerian data will be used to illustrate several phenomena in the impacting vortex-ring dynamics and subsequent incidences on the density stratification in term of internal wave generation.

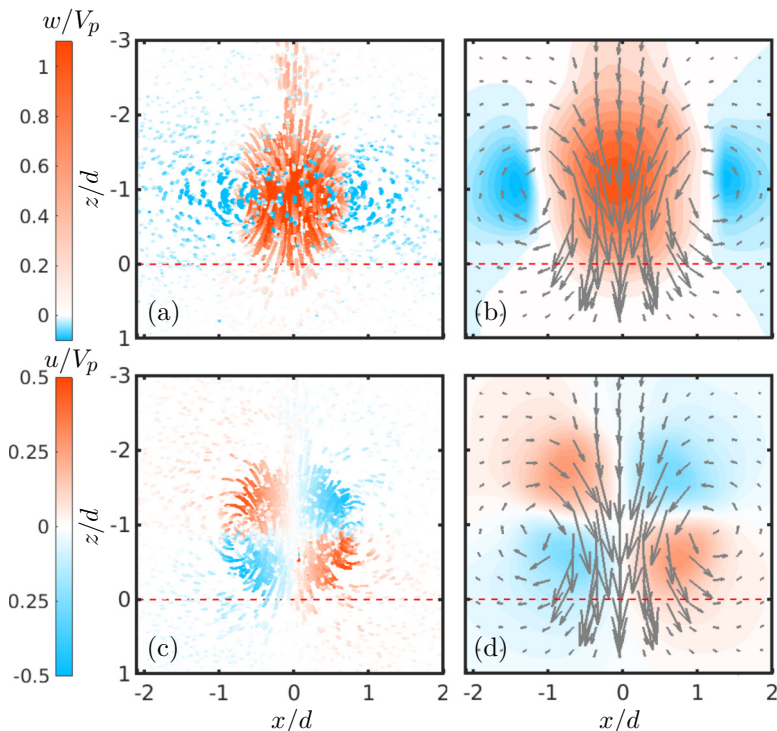


FIG. 5. Vortex-ring (a),(b) vertical and (c),(d) spanwise velocity in the vortex-ring vertical symmetry plane $y/d = 0$ before a normal impact ($\theta = 0^\circ$) with the linear stratification. (a),(c) 25 consecutive particle positions extracted from Lagrangian data on the whole volume depth ($y/d \in [-2.5, 2.5]$) are plotted. (b),(d) Color maps of velocity are derived from Eulerian data, along with the quiver of the velocity (u, w). Velocities and positions are nondimensionalized with the piston velocity V_p and diameter d , respectively.

Figure 5 illustrates Lagrangian (left) and Eulerian (right) representations of the vortex ring impacting the linear stratification normally, with the same velocity component at the same time. Lagrangian trajectory portions show 25 consecutive particle positions preceding the instant at which the Eulerian velocity field is evaluated. During these 25 consecutive images, the vortex ring has traveled over approximately $0.3d$. At this time, the vortical structure is still propagating in the top light homogeneous layer and is centered on $z/d \approx -1$. The two representations are complementary: both sides of the vortex-ring core in this symmetry plane are easily identified on Lagrangian representations at $(x/d, z/d) \approx (\pm 0.8, -1)$, while the vortex-ring symmetry is even more obvious looking at the Eulerian representation.

The initial propagation stage of the vortex ring in the upper homogeneous layer and its eventual impact onto the linear stratification are associated with characteristic timescales that are much shorter than that of internal gravity waves triggered by the vortical impinging structure. The acquisition frequency f_a is fixed for the whole sequence. Nevertheless, the processing frequency has to be adapted in order to ensure a good precision of the measurements by measuring non-negligible displacements of particles (displacements of about five voxels) from the vortex-ring propagation until the internal gravity wave dynamics. In practice, during the vortex-ring first propagation phase, the processing frequency is f_a . Once the vortex ring has reached its maximum penetration depth, 3D fields are processed by tracking positions of particles every $10/f_a$ with an oversampling in time $1/f_a$, and Eulerian projection is computed. In other words, particles in the 3D field n are tracked in the 3D field $n + 10$, particles in the 3D field $n + 1$ are tracked in the 3D field $n + 11$, and so on.

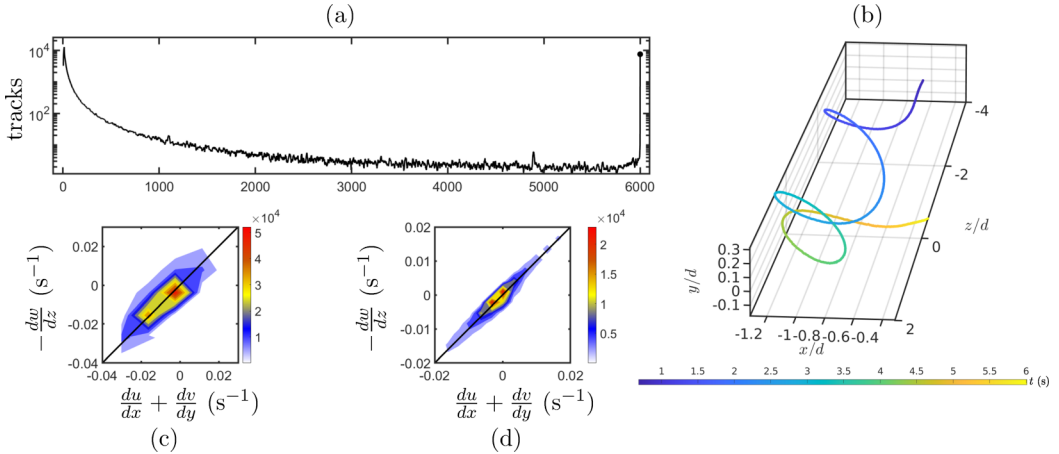


FIG. 6. (a) Histogram of track length (sliding averaged on 10 frames for clarity) in semilogarithmic coordinates. (b) An example of the trajectory colored by the time. Joint PDF of $-\frac{dw}{dz}$ with $\frac{du}{dx} + \frac{dv}{dy}$, (c) before and (d) after vortex-ring interaction with the stratified layer.

Then, taking the benefit of the time over-resolution, up to 10 consecutive computations converted into Eulerian fields are averaged in order to increase the measurement quality.

f. Validation of the 4D-PTV technique. Figure 6(a) shows a histogram of tracked particle trajectory length, or track length. Each detected particle is associated with an identification number as soon as it is tracked in at least $n_{\text{init}} = 4$ consecutive frames. Therefore, the minimum trajectory length is 4 and its maximum is 6000, the total number of frames. As noticed by Schanz *et al.* [29] [see their Fig. 13(a)], most of the tracked particles are detected in only four consecutive frames. The proportion of longer trajectories is lower except for the longest trajectories (6000 time steps long), which represent another extremum of the same order as the shortest trajectories.

Figure 6(b) presents an example of a 697 time-step-long trajectory obtained after the STB calculation. In its early detection, the particle propagates along the z direction with a rectilinear trajectory at approximately $x/d = -0.75$. The particle was chosen close to the vortex-ring axis of symmetry, where the vertical velocity is the highest and mainly vertical. After a while, the particle is dragged by the core of the vortex ring and its trajectory becomes helical. For this peculiar particle, the trajectory ends when it reaches the stratification.

Figures 6(c) and 6(d) present a diagnosis of the Eulerian projection quality through the joint probability density function (PDF) of $-\frac{dw}{dz}$ with $\frac{du}{dx} + \frac{dv}{dy}$ at two specific times in the vortex-ring dynamics: before and after its interaction with the stratification. For an incompressible flow, as is the case in the present study, the velocity divergence is zero and the joint PDF should be concentrated along the first bisector (black line). Here, as noticed in previous studies [35,36], the joint PDF is ellipsoidal due to measurement errors. Finally, errors made on spatial velocity gradients, $E_{\nabla \cdot \mathbf{u}}$, are a combination of the PDF aspect ratio (AR), defined as the ratio of its extension along directions $(x + y)$ and $(x - y)$, respectively, and the rms value of $\nabla \cdot \mathbf{u}$, with

$$E_{\nabla \cdot \mathbf{u}} = \frac{\text{rms}(\nabla \cdot \mathbf{u})}{\sqrt{2} \times \text{AR}}.$$

In Figs. 6(c) and 6(d), the ellipse aspect ratios are, respectively, $\text{AR}_{(c)} \approx 3.5$ and $\text{AR}_{(d)} \approx 6.8$. Rosi and Rival [36] obtained an ellipse aspect ratio $\text{AR} \approx 3$. Thus, it seems that the velocity averaging on 10 consecutive frames realized for the long-term dynamics, i.e., just after the vortex ring enters the stratification, improves the velocity gradient errors. Here, errors on the velocity gradients are $25 \times 10^{-3} \text{ s}^{-1}$ before vortex-ring impacts and $7 \times 10^{-3} \text{ s}^{-1}$ after the impact.

TABLE I. Relevant dimensionless parameters of the present study.

| θ | L/d | $At = (\rho_2 - \rho_1)/(\rho_1 + \rho_2)$ | h/d | $Re = \rho_1 V_p d / \mu$ | $Fr = V_p / Nd$ |
|-----------------------|-------|--|-------|---------------------------|-----------------|
| $[0^\circ, 30^\circ]$ | 3 | 3.85×10^{-2} | 11 | 667 | 1.6 |

C. Control parameters

The setup described previously is characterized by five-dimensional parameters for the fluid environment and four parameters for the vortex-ring generator, including a dimensionless one. Regarding the fluid environment, the parameters are $(\rho_1, \rho_2, h, \mu, g)$, namely, the densities of the lighter and heavier fluid, the thickness of the density stratification, the dynamic viscosity, and the gravity acceleration. Regarding the vortex-ring generator, the parameters are (d, L, V_p, θ) , namely, the generating tube inner diameter, the piston stroke length, the piston velocity, and the launch angle to the vertical. The nine parameters listed above can be expressed with three different units, leading to six dimensionless parameters that are listed in Table I. Also, most of the studies refer to the Richardson number, which compares the gravitational potential energy to the kinetic one, to qualify the vortex-ring and stratification interaction [12,25]. Here, it corresponds to the inverse of the square Froude number, $Ri = 1/Fr^2 = 0.39$.

III. VORTEX-RING PROPAGATION

During the propagation of a vortex ring, the maximal fluid velocity along the propagation axis is reached at the level of the vortex-ring core. Hence, following in time the position of this maximum of velocity is a way to track the vortex-ring trajectory, as was done, for instance, in Advait *et al.* [12].

Here, Lagrangian velocities have to be considered in a zone including the close neighborhood of the vortex-ring propagation axis. For this purpose, a virtual cylinder of diameter d , identical to that of the piston, in line with the vortex-ring launcher of axis \vec{s} , is defined [gray dashed cylinder in the sketch of Fig. 7(a)]. The value of the Lagrangian velocity projected on \vec{s} of all the particles located in this virtual cylinder, $V_{\text{part}_s}(s)$, is computed at each time step. Then, the virtual cylinder is divided into $0.5 d$ long intervals. The total length of the virtual cylinder, which depends on the angle of the

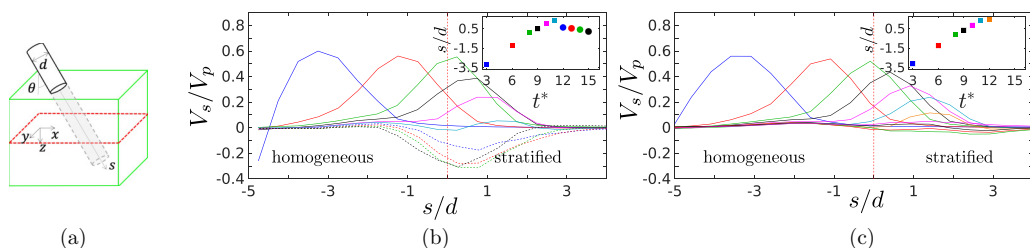


FIG. 7. (a) Sketch of the cylindrical sample volume used to compute the velocity profiles. Axis s is the vortex-ring direction of propagation, the green box represents the lighted fluid volume, the red dashed lines at $s/d = 0$ indicate the stratification upper boundary position, and the gray cylinder represents the volume used for the calculation in line with the vortex-ring launcher. At a given time, particles inside the gray cylinder of diameter d are detected and their Lagrangian velocities are used to establish the mean velocity V_s along s . Time evolution (color) of the velocity profiles V_s along s for (b) $\theta = 0^\circ$ and (c) $\theta = 30^\circ$. Lines are solid when $V_s > 0$ (structure going downwards) and dashed when $V_s < 0$. The top-right inset indicates the velocity extremum position as a function of time (square and circle are used for maximum and minimum, respectively). Note that a given time is associated with a specific color used both for the figure and its inset. V_s , s , and t are normalized by V_p , d , and d/V_p , respectively.

vortex launcher, is divided into 18 intervals s_n with $n = 1, \dots, 18$ for the normal impact and into 24 intervals for the inclined one (s_n with $n = 1, \dots, 24$). The mean velocity $V_s(s_n) = \langle V_{\text{part}_s}(s_n) \rangle$ is evaluated in each interval s_n , without taking into account the relative position of the particles with respect to the cylinder axis. This procedure provides an instantaneous mean velocity profile along \vec{s} , directly issued from the Lagrangian data.

In Fig. 7, velocity profiles are plotted from $t^* = tV_p/d = 3$ (corresponding to the end of the piston stroke) and as long as a coherent structure is detectable.

For the case $\theta = 0^\circ$ [Fig. 7(b)], three phases can be identified. First, the vortex ring propagates in the homogeneous layer with a constant velocity (dark blue, red, and green). Then, the vortex ring slows down as it penetrates the stratification up to $s/d = 1.5$ (black, magenta, and blue). Finally, the vortical structure recoils slowly, as illustrated by the circles in the inset and the corresponding dashed velocity profiles. The Froude number of the present study, $\text{Fr} = 1.6$, corresponds to a penetrative regime for the vortex ring.

For the case $\theta = 30^\circ$ [Fig. 7(c)], after a propagation phase at constant velocity, the vortex ring penetrates the stratification up to $s/d \approx 1.5$, which is approximatively the same distance (but shallower depth) as for the normal impact. For the inclined impact, the mean velocity along \vec{s} remains positive up to $t^* = 12$. Once the vortex-ring dynamics is no longer dominated by inertia, which acts along \vec{s} , the main force is the buoyant one, which acts upwards. Therefore, the recoil of the penetrative structure is not likely to occur along \vec{s} .

This kind of simple projection turns out to be useful, at least for the normal impact, in order to follow the coherent structure trajectory, including its deceleration and return in the stratified region. From this big picture, details on the vortex-ring dynamics and interaction with the stratification at some characteristic times in its lifetime will be addressed through the analysis of the vorticity and velocity fields in the following.

IV. ANALYSIS OF THE VORTICITY FIELD

The forcing of baroclinic vorticity by the penetrative vortex ring and subsequent vorticity reorganization is evaluated in this section. The physical mechanisms leading to the baroclinic vorticity production are explained. In the case of the inclined impact, the collapse of the vortex ring into a vertically flattened dipolar vortex is detailed thanks to the time evolution of vorticity fields in several flow sections.

A. Normal impact ($\theta = 0^\circ$)

In Fig. 8, snapshots of the vorticity were chosen so that the vortex ring descends vertically in the homogeneous upper layer at $t^* = 6$, penetrates the stratification at $t^* = 11$, and goes back upwards at $t^* = 15$. The additional time, $t^* = 20$, corresponds to the decay of the coherent structure.

At $t^* = 6$ [Fig. 8(a)], the isosurface of vorticity highlights a toroidal shape characteristic of the vortex ring. The axisymmetry of the vortical structure can be appreciated through the color maps of vorticity [Fig. 8(b)] picked at the same time in a 2D diametrical plane of the 3D vortex ring. Color maps show two antisymmetric vorticity patches of similar intensity and spatial extension. Moreover, the streamlines of the in-plane components of the velocity, only referred to as streamlines for simplicity in the following, are as well fairly symmetrical with respect to $x/d = 0$. At this early stage, the vertical position of the vortex-ring core, given by the vorticity extrema position, is $z/d = -1.25$. Note that this is in agreement with the location of the maximum axial velocity in Fig. 7(b) ($z/d = -1.2$), with the difference given by the two methods being less than a mesh size.

As the vortex ring enters the stratification and penetrates down to $z/d \approx 1.5$ at $t^* = 11$, the toroidal shape is preserved, although the vortex ring shrinks progressively as it penetrates the stratified layer. The streamlines and vorticity color maps in the vertical symmetry plane highlight vorticity patches of the same intensity, but smaller spatial extent at $t^* = 11$ than at $t^* = 6$. Also, at $t^* = 11$, color maps of the vorticity exhibit an envelope of secondary counter-rotating vorticity

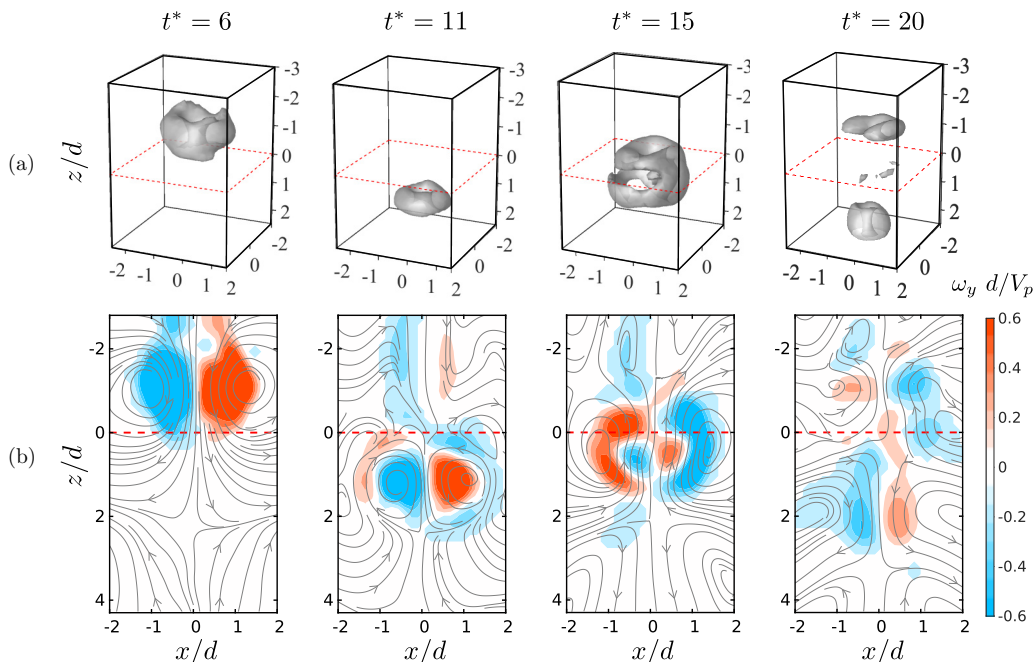


FIG. 8. Vortex ring impacting the stratification vertically at $t^* = [6, 11, 15, 20]$ (columns from left to right). (a) The gray envelope indicates the isosurface of vorticity, $\|\omega\| = 0.5 \omega_{\max}$. (b) Color maps of the nondimensional y component of vorticity $\omega_y d/V_p$ are shown in the vertical symmetry plane $y/d = 0$, and gray lines are associated with the in-plane components of the velocity streamlines in the laboratory reference frame. The red dashed line marks the stratification upper boundary.

enclosing the primary vortex ring. This secondary vorticity is generated through baroclinic effects. As the vortex ring penetrates into the stratification, isopycnals, which are originally horizontal, are locally deformed. In addition, in the scope of the Boussinesq approximation (small At number), the pressure field is essentially hydrostatic and, consequently, isobars are and remain horizontal. Therefore, considering the vorticity equation,

$$\frac{d\boldsymbol{\omega}}{dt} = (\boldsymbol{\omega} \cdot \nabla)\mathbf{u} + \underbrace{\frac{1}{\rho} \nabla \rho \times \mathbf{g}}_{\dot{\boldsymbol{\omega}}_b} + \nu \nabla^2 \boldsymbol{\omega},$$

where \mathbf{g} is the gravity acceleration, the pressure and density gradients become misaligned and the baroclinic production $\dot{\boldsymbol{\omega}}_b$ is triggered during the vortex-ring penetration. Figure 9 presents a schematic of the baroclinic vorticity generation mechanism for a normal impact. The orientation of the density gradient, and in particular the sign of its horizontal component, will drive the sign of the generated baroclinic vorticity. It follows that the resulting baroclinic vorticity, made of vorticity of opposite sign, should shield the primary vortex ring and exhibit the same axis of symmetry, $x/d = y/d = 0$. This feature is observed in Fig. 8(b).

The deformation of isopycnals can be interpreted from $t^* = 6$ by considering the streamlines below the stratification that indicate a hyperbolic point at $z/d \approx 2.5$. The velocity field associated with a vortex ring evolving in a homogeneous fluid always exhibits a hyperbolic point along the axis of symmetry at the front of the vortical structure. Here, the fact that this hyperbolic point sits in the stratification at $t^* = 6$, while the vortex-ring core is still in the upper homogeneous layer at this stage, indicates that the vortical structure starts to act on the stratification, pushing isopycnals downwards, even before the vortex core enters the stratified layer. This observation is corroborated

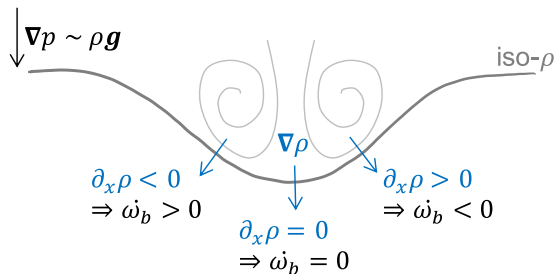


FIG. 9. Schematic of the mechanism of baroclinic vorticity generation by a normal impact of a vortex ring on a density stratification.

by that of Fig. 7(b), where vertical velocities are measured in the upper part of the stratification ($z/d \in [0, 1]$). In contrast, in Fig. 7(b), from $t^* = 3$ to $t^* = 6$, the velocity profile does not show any significant change. Thus, at this stage, the vortex ring perturbs the stratification which, however, does not influence, in return, the vortex-ring dynamics.

The baroclinic vorticity envelope surrounding the vortex ring has the effect of peeling away the primary vorticity. This leads to the shrinking of the primary vortex ring, as was previously observed in the cases of two-layer stratifications [13,26,27], of a thin linear stratification [12], and of a deep continuous stratification [37]. At $t^* = 15$, the primary vortex ring has shrunk and is weaker, while baroclinic vorticity is now the main vortical structure (see Fig. 8). Hence, at this stage, the gray isosurface of vorticity [see Fig. 8(a) at $t^* = 15$], associated with the mid value of the maximum of vorticity, surrounds the baroclinic vorticity instead of the primary structure. Such an intense baroclinic envelope was also observed in the three-dimensional reconstruction of Olsthoorn and Dalziel [13]. The complete vortical structure goes back upwards and is located at this stage at $z/d \approx 0.5$, in agreement with the peak of negative velocity along the vortex-ring axis in Fig. 7(b). The rise of the coherent structure can be explained by two concomitant effects. From a dynamical point of view, the fluid composing the vortex ring is lighter than the local stratification and buoyancy effects act vertically to make the structure go up. From a kinematical point of view, streamlines show that in the close neighborhood of the vortex ring, the velocity field induced by the baroclinic vorticity envelope is directed upwards.

At $t^* = 20$, both the vortex ring and the envelope of baroclinic vorticity have decayed and only residual weak vorticity remains. Two weak coherent patches of vorticity are detected at $z/d = 2$, but streamlines do not roll up around these vorticity patches. Thus, at this location, vorticity patches are not associated with rotation but with shear.

To conclude, for the vertical impact ($\theta = 0^\circ$), at the specific Froude number considered in the present study, the vortex ring enters the stratification up to $z/d \approx 1.5$. During the ring descent in the stratified layer, baroclinic vorticity is generated and forms a counter-rotating shield surrounding the primary vortical structure. The interaction of this newly generated vorticity with the primary vortex ring has the effect of shrinking the impinging ring, stopping and pushing it back upwards in the homogeneous light layer. Note that the streamlines inside the stratification present at all times a symmetry with respect to $x/d = 0$ in the vertical symmetry plane, while they are no longer coherent in the upper homogeneous zone at a late stage.

B. Inclined impact ($\theta = 30^\circ$): From donut to pancake

For the inclined impact, the vortex ring quickly loses its coherence and the 3D isovorticity surfaces do not reveal much on the global dynamics. The loss of axisymmetry can be analyzed by considering vorticity fields in two orthogonal planes: the vertical symmetry plane $y/d = 0$, and a horizontal plane at a given z/d in the stratified region (see Figs. 10). The vertical position of the

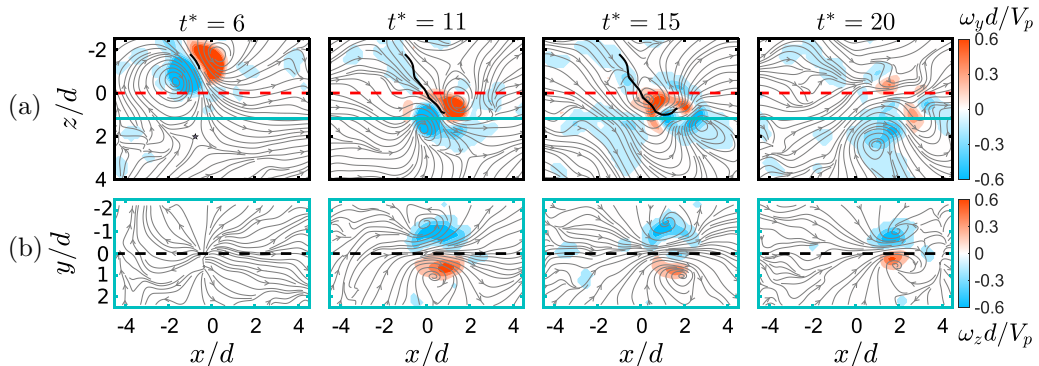


FIG. 10. Vortex ring impacting the stratification with an angle $\theta = 30^\circ$ to the vertical at $t^* = [6, 11, 15, 20]$ (columns from left to right). (a) Color maps show nondimensional horizontal vorticity in the vertical symmetry plane $y/d = 0$. Solid thick black lines give the trajectory followed by the vortex ring. (b) Color maps represent nondimensional vertical vorticity in the horizontal plane $z/d = 1.3$. Gray lines in rows (a) and (b) are associated with streamlines in the laboratory reference frame. The star in the top left figure points out a hyperbolic point at $(x/d, z/d) \approx (-1, 2)$. The red dashed line in (a) marks the stratification upper boundary and the cyan solid line indicates the position of the horizontal plane $z/d = 1.3$. The black dashed line in (b) marks the vertical symmetry plane $y/d = 0$.

horizontal plane was chosen to be close to the maximum depth reached by the impacting vortical structure [see Fig. 7(c)].

At $t^* = 6$, in Fig. 10(a), color maps of horizontal vorticity show the vortex ring just before it enters the stratification. The primary vortical structure is compact and close to being symmetrical around its axis. At this time, streamlines in both the vertical and the horizontal planes highlight the signature of the vortex ring approaching the stratification. In the vertical symmetry plane, a hyperbolic point is identified at $(x/d, z/d) \approx (-1, 2)$ and indicated by a star. In the horizontal plane, streamlines of the in-plane velocity radiate away from $(x/d, y/d) = (-0.5, 0)$.

At $t^* = 11$, the vortex ring has completely entered the stratified layer. In the vertical symmetry plane, negative baroclinic vorticity is generated in front of the primary structure, just below the red vorticity patch, while positive secondary vorticity, although weaker, appears on the top left of the blue vorticity patch. Figure 11(a) presents a schematics of the isopycnal deformation and the subsequent baroclinic vorticity generation for the inclined impact. The shape of the isopycnal surrounding the vortex ring in the symmetry plane could be approximated by an upside-down bell shape skewed to the right. For the inclined impact, contrary to the normal one, the vertical minimum of the surrounding isopycnal (corresponding to zero horizontal density gradient) is no longer aligned with the vortex-ring axis of symmetry. Therefore, in the vertical plane $y/d = 0$, the lower part of the vortex ring (blue patch) generates baroclinic vorticity of opposite sign on its left and on its right.

For an inclined impact, the primary vortex-ring vorticity has a vertical component proportional to $\sin \theta$, while the vorticity was purely horizontal in the case of the normal impact. Furthermore, when the primary structure enters the stratification, its vorticity reorganizes with the baroclinic vorticity generated. The lower part of the vortex ring [i.e., blue patch in Fig. 10(a)] merges with the baroclinic vorticity of the same sign on its right and is eroded by the baroclinic vorticity of opposite sign on its left part, while the upper part of the ring is barely affected by the baroclinic vorticity at $t^* = 11$. Then, at $t^* = 15$, the upper part of the vortex ring is observed to merge with the baroclinic vorticity of the same sign close to the stratification upper boundary. As shown schematically in Fig. 11(b), these coupled mechanisms make the whole vortical structure tilt counterclockwise, increasing the tilt angle θ . As a result, the vertical component of the vorticity increases. At the same time, two coherent counter-rotating patches of vertical vorticity can be identified in the horizontal plane $z/d =$

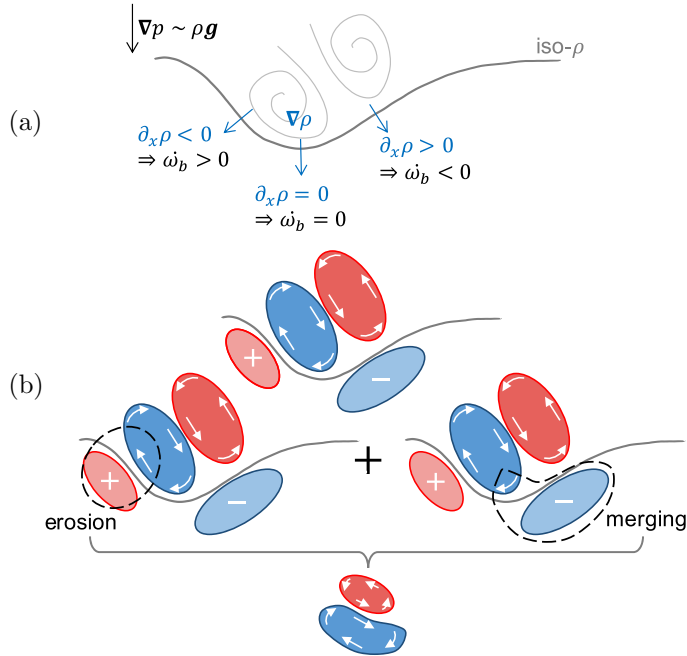


FIG. 11. (a) Schematics of the mechanism of baroclinic vorticity generation by an inclined impact of a vortex ring on a density stratification. (b) Schematics of the subsequent vorticity organization after erosion and merging of the vortex ring with the baroclinic vorticity.

1.3 [see Fig. 10(b) at $t^* = 11$]. This vorticity signature is fairly symmetrical with respect to $y/d = 0$ and the streamlines, associated with the vorticity-induced velocity field, show a global motion of the coherent structure towards positive x/d .

At $t^* = 15$, streamlines show that the reorganized vorticity is principally translating horizontally along the x direction. At this stage, the vorticity field in the horizontal section plane remains well defined and symmetrical, whereas the original vortex ring is barely identifiable in the vertical symmetry plane.

Later, at $t^* = 20$, the vortex structure in the vertical plane is even more disintegrated and only residual vorticity remains. Yet, in the horizontal plane, the vertical vorticity is still coherent, compact, and, at this stage, stronger than the vorticity measured in the vertical plane.

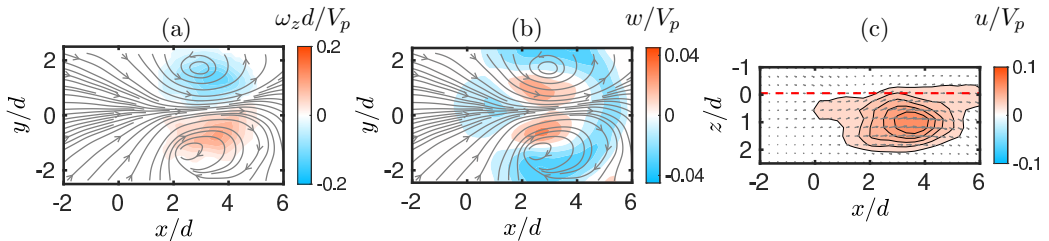


FIG. 12. (a) Nondimensional vertical vorticity field $\omega_z d/V_p$ and (b) vertical velocity field w/V_p in the horizontal plane $z/d = 1$ and (c) horizontal velocity field u/V_p in the vertical symmetry plane $y/d = 0$ for an inclined vortex ring impact at $t^* = 40$. For each figure, (a),(b) gray streamlines and (c) arrows correspond to the in-plane velocity field.

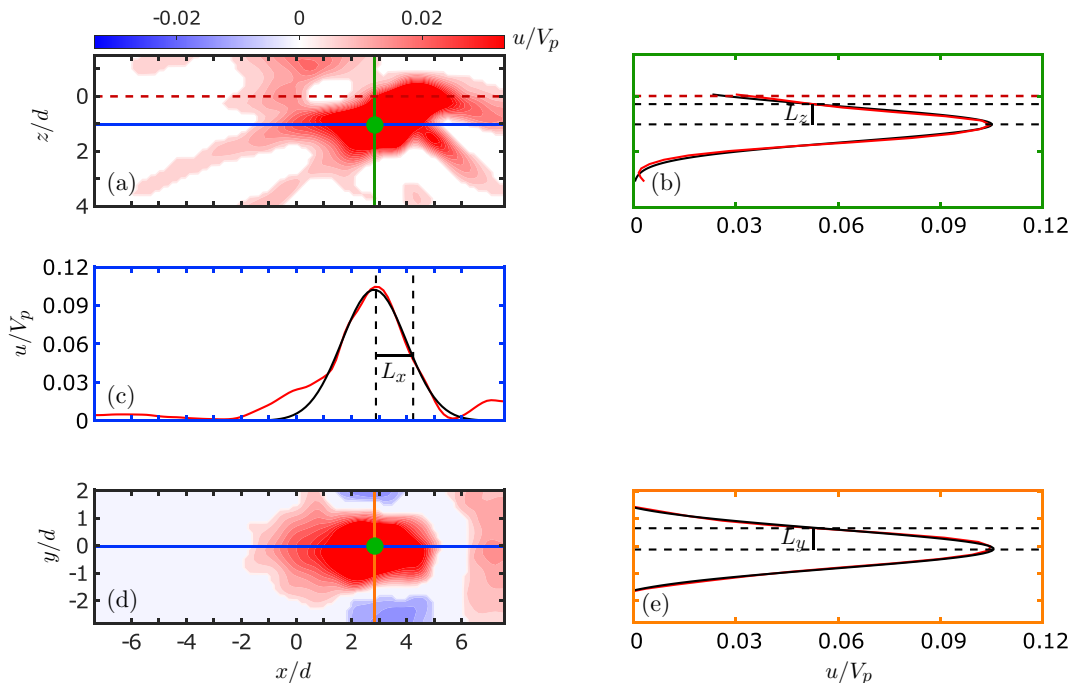


FIG. 13. Characteristics of the vortex dipole at $t^* = 45$ or, equivalently, at $Nt = 28$. Horizontal velocity field u/V_p , (a) in the vertical symmetry plane $y/d = 0$ and (d) in the horizontal plane $z/d = 1.05$. The green dot located at $(x/d, y/d, z/d) = (2.85, 0, 1.05)$ marks the position of the horizontal velocity maximum. (c),(e),(b) Horizontal velocity profiles plotted along lines containing the green dot and directed by x [blue line in (a) and (d)], y [orange line in (d)], and z [green line in (a)], respectively. Horizontal profiles are fitted with a Gaussian function centered on the maximum horizontal velocity position (black curves).

Figure 12(a) shows the vertical vorticity field in the horizontal plane $z/d = 1$ at $t^* = 40$. At this stage, as seen in Fig. 10, the vortex ring launched with an angle $\theta = 30^\circ$ to the vertical has turned into a vortical structure mainly composed of vertical vorticity that propagates to the right. Figures 12(b) and 12(c) show, respectively, the vertical w/V_p and the horizontal velocity field u/V_p in the horizontal plane $z/d = 1$ and in the vertical symmetry plane $y/d = 0$ at the same time. Figure 12(c) allows determination of the vertical and streamwise extent of the sliding vortex structure. At this stage, the initial three-dimensional toroidal structure has turned into a flattened pancakelike dipolar vortex that extends horizontally from $x/d = 1$ to $x/d = 5.5$ and vertically from $z/d = 0$ to $z/d = 2$. This kind of flow flattening under the effect of density stratification was previously observed, for instance, by Voropayev *et al.* [38,39], who have experimentally shown that the background stratification imposes a vertical constraint on the flow, inhibiting vertical motions. Figure 12(b) is representative of the vertical velocity field in any horizontal plane $z/d \in [0, 2]$ and indicates that at this specific time, the water column is going upwards close to the vortex dipole cores and downwards all around the propagating vortex structure and, in particular, at its front.

Characteristics of the dipolar vortical structure are highlighted in Fig. 13 at $t^* = 45$ or, equivalently, at $Nt = 28$. At this time, the flow reorganization leading to the generation of a quasi-two-dimensional vortex dipole is over. Figures 13(a) and 13(d) show the horizontal velocity component u/V_p in the vertical symmetry plane $y/d = 0$ and in the horizontal plane $z/d = 1.05$, respectively. Velocity fields present a flow mainly aligned with x and color maps in the vertical symmetry plane exhibit beams connected to the dipole. In the horizontal plane, the horizontal

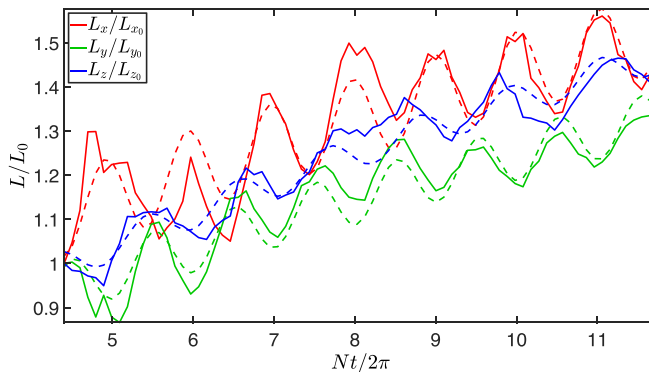


FIG. 14. Time evolution of the vortex dipole characteristic dimensions (solid lines) and fit of the experimental data with a function $L_i/L_{i0} = a_i\sqrt{v(t - b_i)} + c_i \cos(d_i t + e_i)$ with $i = \{x, y, z\}$ (dashed lines).

component of the velocity is mainly positive close to the symmetry plane ($y/d \in [-1, 1]$) and negative beyond, which is proper to the velocity field of a vortex dipole.

Profiles of the horizontal velocity component along the three directions of space and containing the maximum velocity position $(x/d, y/d, z/d) = (2.85, 0, 1.05)$ are plotted in Figs. 13(b), 13(c) and 13(e). Velocity distributions are approximated by a Gaussian function as had already been done for vortex dipoles evolving in a density stratification [40,41]. The Gaussian fits are adjusted over a range of $4d$ on either side of the maximum velocity position. The vortex dipole extensions along x , y , and z , respectively, L_x , L_y , and L_z , are computed from the velocity profiles as the half width at half height of the Gaussian distributions [see Figs. 13(b), 13(c) and 13(e)]. Dimensions of the dipole structure at this time are used in the following as reference lengths and are indexed with a 0: $L_{x0}/d = 1.45$, $L_{y0}/d = 0.84$, and $L_{z0}/d = 0.73$.

The time evolution of the vortex dipole characteristic dimensions (nondimensionalized by their reference value) is presented in Fig. 14. The characteristic dipole dimension increases with time in the three directions. This was previously observed for thin vortex dipoles directly generated in linearly stratified fluid [42] for which the spreading is due to viscous effects [40]. In the present case, in addition to the overall spread of the structure, large amplitude oscillations are measured in the three directions of space. Those two concomitant phenomena are taken into account by an adjustment of the experimental data with the following function: $L_i/L_{i0} = a_i\sqrt{v(t - b_i)} + c_i \cos(d_i t + e_i)$, where $i = \{x, y, z\}$ (dashed lines in Fig. 14). Oscillation frequency can be evaluated through the d_i coefficient of this function. It results that whatever the spatial direction, the value of the frequency oscillation is always $d_i = 1.8 \pm 0.1 \text{ rad s}^{-1}$, which is close to the stratification buoyancy frequency ($N = 1.88 \text{ rad s}^{-1}$). It can also be noted that the oscillations in the x direction are out of phase with those in the two other directions. The vortex dipole characteristic length scale oscillations are measured at a frequency driven by the background stratification, and streamwise expansions (contractions) correspond to spanwise and vertical contractions (expansions) to ensure volume conservation. Nevertheless, we could not yet provide an unequivocal explanation of the mechanism behind the vortical structure beating.

V. INTERNAL GRAVITY WAVE GENERATION

As the vortex ring penetrates the stratification, it pushes isopycnals downwards. The density stratification, initially at rest, is therefore perturbed, leading to oscillations of fluid particles inside the stratification to return to their initial hydrostatic position. This behavior is highlighted in Fig. 15, where isosurfaces of positive (red) and negative (blue) radial and vertical velocity are shown just after the vortex ring has reached its maximum penetration depth in the case of a normal impact.

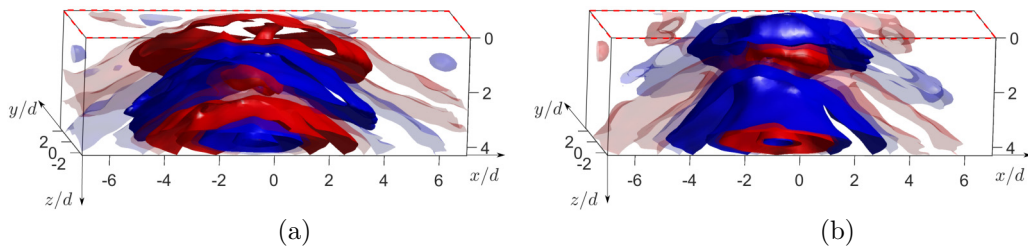


FIG. 15. Isosurfaces of (a) radial and (b) vertical velocity in the stratified zone subsequent to the vertical impact ($\theta = 0^\circ$) of the vortex ring at $t^* = 35$ (equivalently, $Nt = 22$). Red isosurfaces correspond to (a) radial velocities from the line $x/d = y/d = 0$ or (b) downward velocities, while blue isosurfaces correspond to velocities oriented the other way around. The red dashed line points to the stratification upper boundary $z/d = 0$.

Figure 15 exhibits coaxial conical layers associated with velocities of alternating orientations. These conical isosurfaces can be attributed to internal waves as a response of the stratification to the impact of the vortex ring. Indeed, in the experiment of Mowbray and Rarity [15], a bar oscillating vertically at a given frequency ω in an ambient density stratification initially at rest triggers four beams of waves emanating from the cylinder in a vertical plane of symmetry. This particular organization of the velocity field in the surrounding of the cylinder is referred to as the St Andrew's cross. In the case of an oscillating sphere, the wave beams are contained in two finite-thickness conical shells, with a vertical axis of symmetry including the sphere center. The cone angle α or, equivalently, the St Andrew's cross angle to the vertical was shown to be coupled with the oscillation frequency ω and the buoyancy frequency N through the following dispersion relation [14]:

$$\omega/N = \cos(\alpha).$$

In the present study, the perturbation associated with the vortex-ring impact is not monochromatic as was the case for the sphere experiment. Nevertheless, the velocity field in the stratification is organized into several clearly defined coexisting coaxial cones with various angles to the vertical. In the following, the buoyancy frequency N , which is the characteristic frequency for the internal gravity waves, will be used to make time nondimensional. For the launch angles considered here, the front of the vortex ring reaches the upper boundary of the stratification at $t^* = 6$, which corresponds to $Nt = 3.7$, then the maximum penetration depth is reached at $t^* = 11$ or, equivalently, at $Nt = 6.7$. Figure 15 corresponds to $Nt = 22$, or $t^* = 35$.

An analysis of the frequency content after a vortex-ring impact onto the stratification was achieved by use of a frequency filtering of the velocity field. For this analysis, only the stratified zone is considered (namely, $z/d \geq 0$) from $Nt = 10$ until $Nt = 70$, which defines a time series of three-dimensional velocity fields. A temporal fast Fourier transform (FFT) is computed on this time series and the Fourier components of the velocity field are thus a function of the associated frequency ω/N . The global power spectrum of the velocity in Fig. 16(a) is obtained by a spatial average of power spectra computed at each location. It presents the highest levels of energy in the range $\omega/N \in [0, 1]$, as expected for internal gravity waves. For the normal impact, the energy is more or less uniformly distributed in this range. The power spectrum for the inclined impact, on the contrary, brings out a peak at $\omega/N = 0$, which is a signature of the coherent motion associated with the horizontally propagating vortex dipole. Then, the FFT output is convoluted with a gate signal in frequency of thickness $\Delta\omega/N = 0.1$ centered on 10 values of ω/N linearly distributed in $[0, 1]$. For each value of ω/N considered here, an inverse FFT is then computed on the frequency-filtered data set and the resulting velocity field at $Nt = 40$ (intermediate time of the time series) is reconstructed. Figures 16 shows the resulting velocity fields after convolution with a frequency gate signal centered

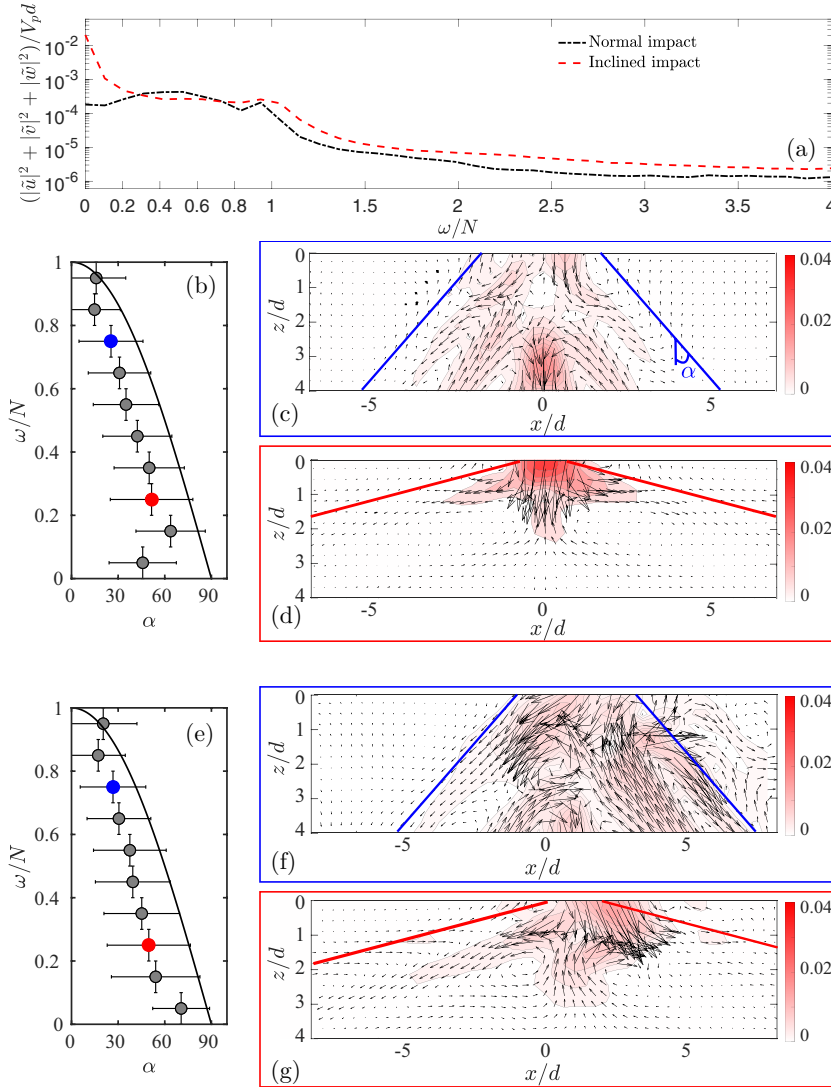


FIG. 16. (a) Power spectrum of the velocity. After convolution of the FFT output with a bandpass filter, for each frequency band, the mean velocity angle α with respect to the vertical for $z/d \geq 0$ at $Nt = 40$ is computed for (b) the normal impact and (e) the inclined one. Black lines show the analytical internal gravity wave dispersion relation for comparison. The vertical error bar extension is the frequency bandwidth $\Delta\omega/N = 0.1$, and the horizontal one is twice the angle standard deviation. (c)–(f) Velocity field filtered at the frequency $\omega/N = 0.75$ in the vertical symmetry plane $y/d = 0$ for the normal and inclined vortex-ring impacts, respectively. (d)–(g) Similar to (c) and (f) for $\omega/N = 0.25$. The color field is the velocity magnitude normalized by the piston velocity. The red (blue) solid line is aligned with the internal wave beam angle expected for $\omega/N = 0.25$ ($\omega/N = 0.75$).

on $\omega/N = 0.25$ [Figs. 16(d) and 16(g)] and on $\omega/N = 0.75$ [Figs. 16(c) and 16(f)] in the vertical symmetry plane $y/d = 0$. These figures actually highlight some specific velocity angles to the vertical depending on the filtering frequency. The red and blue solid lines in Figs. 16(c), 16(d), 16(f), and 16(g) show the direction predicted by the dispersion relation for an internal wave beam associated with a forcing oscillation $\omega/N = 0.25$ and $\omega/N = 0.75$, respectively. These lines are

indeed parallel to the isovelocity-magnitude directions. Nevertheless, note that the velocity field still presents at $Nt = 40$ a strong component aligned with the initial vortex-ring propagation axis direction.

In order to make these observations more quantitative, the velocity angle with regard to the vertical, α , is evaluated at each mesh grid point of the frequency-filtered velocity field, resulting in a map of α values. The mean value of α is assumed to be the angle corresponding to the frequency ω/N considered and is represented by a circle in Figs. 16(b) and 16(e). The standard deviation of α gives the horizontal extension of the error bar, while the vertical extension is simply the frequency bandwidth. Independently of the vortex-ring launch angle, there is a correct agreement between the angle obtained after the filtering and the one predicted by the internal wave dispersion relation. The discrepancies between the measured mean angles α and the internal waves dispersion relation along with the large horizontal extension of the error bars can be attributed to at least two effects. First, the strong velocity aligned with the vortex-ring propagation direction adds an important contribution to the mean angle α . Next, when two beams cross each other, trajectories curve at their intersection and velocity vectors of multiple directions exist in these zones. Nevertheless, Fig. 16 indicates that waves triggered by the impacting vortex ring are indeed internal gravity waves, whatever the impact angle to the vertical, and that all the frequencies $\omega/N \in [0, 1]$ are triggered.

In the present case, the strength of the wave source is diminishing as the vortex ring decelerates and shrinks. As a result, internal gravity waves are unsteady. At $Nt = 70$, cone angles are close to $\alpha = 0^\circ$ (not shown here) and the remaining frequency is very close to the buoyancy frequency. Since the group velocity is a decreasing function of the frequency ω (the dominant wave number being fixed by the vortex-ring dimension), the energy of the waves at low frequencies (i.e., large cone angles α) radiates away faster than the one associated with high-frequency waves (i.e., small cone angles α). Hence, the dominant wave features in the fixed volume considered here are cones whose angle reduces with time.

For a more precise description of internal waves behavior, the left column of Fig. 17 shows the time evolution of isosurfaces of constant vertical velocity in the horizontal plane $z/d = 2$ after a vertical [Fig. 17(a)] and an inclined [Fig. 17(c)] impact. The position of the horizontal plane is chosen below the maximal penetration depth reached by the vortex ring in order to avoid coherent motions directly associated with the vortex ring and to focus on radiated waves. Whatever the vortex-ring propagation angle to the vertical, from the early stage of the impact until $Nt = 70$ (which corresponds to $t^* = 111.7$), alternating negative (blue) and positive (red) vertical velocities are measured in the stratification, a signature of persistent internal gravity waves. Figures 17(b) and 17(d) give the quantitative time evolution of the vertical velocity at three positions in the horizontal plane $z/d = 2$: $(x/d, y/d) = (0, [-1, 0, 1])$ for the normal impact [Fig. 17(b)] and $(x/d, y/d) = (2, [-1, 0, 1])$ for the inclined one [Fig. 17(d)] in order to get a measure in the vertical symmetry plane and one diameter away from the vortex-ring vertical symmetry plane $y/d = 0$ on each side of this plane. In Figs. 17(a) and 17(c), the vertical plane $y/d = 0$ is shown by a translucent plane in order to highlight any possible break of symmetry with respect to this plane.

For the normal impact [Fig. 17(a)], at a fixed time, the disklike structure of the vertical velocity result from the intersection of the horizontal plane $z/d = 2$ with the multitude of coaxial cones radiated after the vortex-ring impact. The disk radius decreases with time, and at late times, the area where the vertical velocity component remains non-negligible is localized very close to the initial vortex-ring propagation axis ($x/d = y/d = 0$). Toroidal structures of weaker amplitudes are also visible, centered around this point, corresponding to a truncation of the cones associated with radiating internal waves with larger angles. In accordance with this observation, Fig. 17(b) shows that the maximum vertical velocity magnitude is measured on the vortex-ring symmetry axis. A fairly good symmetry is measured on each side of the vertical symmetry plane $y/d = 0$. The unsteady behavior of the waves can also be appreciated through the decrease in time of the velocity magnitude.

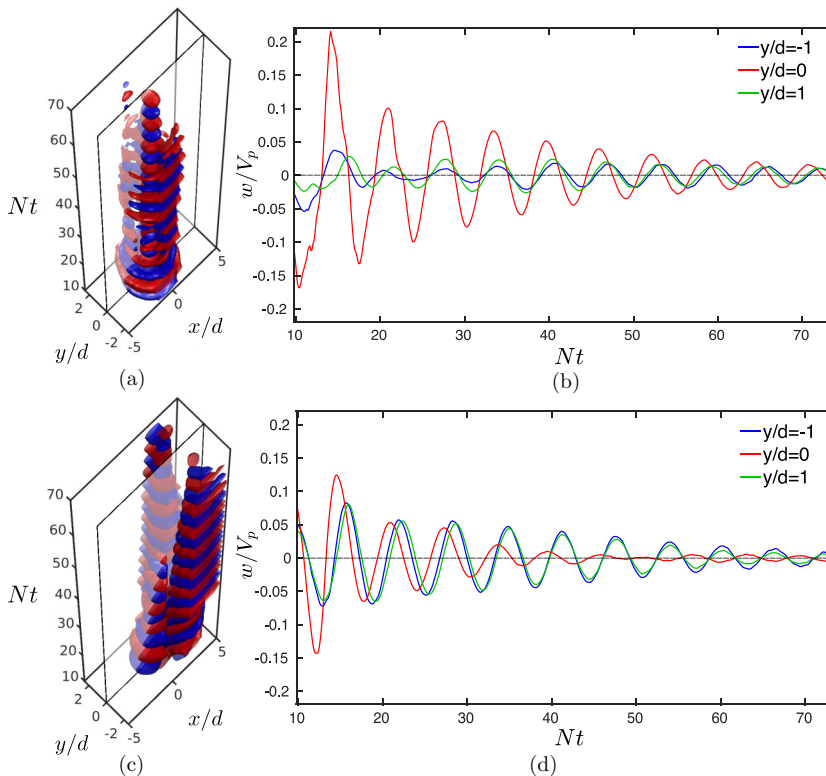


FIG. 17. Spatiotemporal diagram of vertical velocity in the horizontal plane $z/d = 2$ for the (a) normal and (c) inclined impact. (b) Time evolution of the vertical velocity for the normal impact at $(x/d, z/d) = (0, 2)$ and three different spanwise locations. (d) Time evolution of the vertical velocity for the inclined impact at $(x/d, z/d) = (2, 2)$ and three different spanwise locations.

For the inclined impact [Figs. 17(c) and 17(d)], up to $Nt = 30$ (i.e., up to $t^* = 49$), the vertical velocity magnitude is about the same at the three spanwise positions $y/d = -1, 0$, and 1 along the line $x/d = 2$ [Fig. 17(d)]. At a later stage ($Nt > 40$), the velocity magnitude collapses in the symmetry plane, while two symmetric branches of non-negligible and nearly equal velocity are maintained on either side of the symmetry plane, one diameter away from it. For $Nt > 28$, the coherent dynamics resulting from the vortex-ring reorganization into a dipolar vortex is quasi-two-dimensional, as shown in Figs. 12 and 13. On the other hand, internal gravity waves are associated with background radial and vertical motions. By comparing Figs. 12(a) and 12(b) with Fig. 17(c), we observe that the two symmetric branches of vertical velocity are located at the vortex dipole cores. Once the vertically flattened vortex dipole is generated, internal waves are observed to radiate from the dipolar structure cores.

Note that whatever the launch angle, the velocity magnitude is more or less the same, i.e., between 2 and 10% of the piston velocity. Moreover, there is a symmetry of the wave amplitude and phase on either side of the vertical symmetry plane (blue and green lines), but the oscillations in the symmetry plane (red line) are in phase quadrature.

VI. CONCLUSION

The dynamics of a vortex ring generated in a light homogeneous fluid and impacting a density stratification was experimentally studied using a time-resolved 3D-PTV technique. The technique,

along with the specific setup of the experiment, have been presented. The vortex ring was launched with two different angles θ relative to the vertical, namely, $\theta = 0^\circ$ and $\theta = 30^\circ$. The time evolution of the impacting vortical structure, the baroclinic vorticity production, and the internal gravity wave generation have been addressed for both configurations.

For the normal impact ($\theta = 0^\circ$), the vortex-ring propagation and structure maintain axial symmetry throughout their evolution. When the vortex ring penetrates the density stratification, misalignment of isopycnals and isobars produces counter-rotating baroclinic vorticity with respect to the primary vorticity. The primary vortical structure, surrounded by the baroclinic vorticity, then shrinks and recoils upwards due to buoyant effects and the interaction with the secondary vorticity. In parallel and until the end of the time series presented here, internal gravity waves are triggered by the impact of the vortex ring on the stratification and are shown to contain the whole spectrum of frequency $\omega \in [0, N]$, where N is the stratification buoyancy frequency. In the stratified region, the 3D measurements reveal the expected conical structure.

For the inclined impact, the loss of axisymmetry is observed as the vortex ring penetrates the stratification. In this configuration, secondary baroclinic vorticity, produced from the moment the lower part of the vortex ring enters the stratification, is not uniformly distributed around the primary structure. Once the vortex ring has completely penetrated the stratification, the upper part of the vortex ring interacts with the baroclinic vorticity previously triggered. This leads to a tilting and flattening of the vortical structure in the vertical direction. The resulting vortical structure is mainly composed of two counter-rotating poles of vertical vorticity. As this vortex dipole propagates horizontally and spreads, its characteristic dimensions oscillate at a frequency close to the buoyancy frequency. For the inclined impact, internal gravity waves are radiated in all directions, i.e., for the whole spectrum of frequency (as was the case for the normal impact). Nevertheless, the wave intensity is no longer uniform in coaxial conelike structures and two intense branches emerge on either side of the vertical symmetry plane and at the location of the dipolar vortex poles. One has to keep this flow reorganization in mind to interpret the dynamics of inclined impacts onto a stratification if measurements are only realized in the vertical symmetry plane.

This work shows the importance of the impacting angle θ to the vertical. Knowing now the global reorganization behavior, a complementary parametric study on the influence of this parameter will be of great interest. In particular, this future work could address the existence of a threshold angle for the tilting and subsequent flattening of the primary vortex ring.

ACKNOWLEDGMENTS

The authors would like to thank the FERMAT federation (FR 3089, Université de Toulouse, France) for the technical support with the 4D tomo PIV equipment (funded by the CPER I-MATECBIO). We further thank Matthieu Mercier for fruitful discussions on internal gravity waves and two anonymous reviewers for their constructive comments on the manuscript that helped to improve the presentation of this work.

-
- [1] B. Dintrans, A. Brandenburg, A. Nordlund, and R. F. Stein, Spectrum and amplitudes of internal gravity waves excited by penetrative convection in solar-type stars, *Astron. Astrophys.* **438**, 365 (2005).
 - [2] G. V. Lauder and E. G. Drucker, Forces, fishes, and fluids: Hydrodynamic mechanisms of aquatic locomotion, *Physiology* **17**, 235 (2002).
 - [3] P. F. Linden and J. S. Turner, “Optimal” vortex rings and aquatic propulsion mechanisms, *Proc. R. Soc. Lond. B* **271**, 647 (2004).
 - [4] D. An, A. Warning, K. G. Yancey, C.-T. Chang, V. R. Kern, A. K. Datta, P. H. Steen, D. Luo, and M. Ma, Mass production of shaped particles through vortex ring freezing, *Nat. Commun.* **7**, 12401 (2016).
 - [5] S. C. Shadden, J. O. Dabiri, and J. E. Marsden, Lagrangian analysis of fluid transport in empirical vortex ring flows, *Phys. Fluids* **18**, 047105 (2006).

- [6] C. Cummins, M. Seale, A. Macente, D. Certini, E. Mastropaolo, I. M. Viola, and N. Nakayama, A separated vortex ring underlies the flight of the dandelion, *Nature (London)* **562**, 414 (2018).
- [7] T. Maxworthy, The structure and stability of vortex rings, *J. Fluid Mech.* **51**, 15 (1972).
- [8] T. Maxworthy, Some experimental studies of vortex rings, *J. Fluid Mech.* **81**, 465 (1977).
- [9] S. E. Widnall, D. B. Bliss, and C.-Y. Tsai, The instability of short waves on a vortex ring, *J. Fluid Mech.* **66**, 35 (1974).
- [10] P. G. Saffman, The number of waves on unstable vortex rings, *J. Fluid Mech.* **84**, 625 (1978).
- [11] K. Shariff and A. Leonard, Vortex rings, *Annu. Rev. Fluid Mech.* **24**, 235 (1992).
- [12] S. Advaita, K. V. Manu, A. Tinaikar, U. K. Chetia, and S. Basu, Interaction of vortex ring with a stratified finite thickness interface, *Phys. Fluids* **29**, 093602 (2017).
- [13] J. Olsthoorn and S. B. Dalziel, Three-dimensional visualization of the interaction of a vortex ring with a stratified interface, *J. Fluid Mech.* **820**, 549 (2017).
- [14] M. J. Lighthill, *Waves in Fluids* (Cambridge University Press, Cambridge, 1978).
- [15] D. E. Mowbray and B. S. H. Rarity, A theoretical and experimental investigation of the phase configuration of internal waves of small amplitude in a density stratified liquid, *J. Fluid Mech.* **28**, 1 (1967).
- [16] D. G. Hurley and G. Keady, The generation of internal waves by vibrating elliptic cylinders. part 2. approximate viscous solution, *J. Fluid Mech.* **351**, 119 (1997).
- [17] B. Voisin, E. V. Ermanyuk, and J.-B. Flor, Internal wave generation by oscillation of a sphere, with application to internal tides, *J. Fluid Mech.* **666**, 308 (2011).
- [18] E. Ermanyuk, N. Shmakova, and J. B. Flor, Internal wave focusing by a horizontally oscillating torus, *J. Fluid Mech.* **813**, 695 (2017).
- [19] J. K. Ansong and B. R. Sutherland, Internal gravity waves generated by convective plumes, *J. Fluid Mech.* **648**, 405 (2010).
- [20] A. Brandt and K. R. Shipley, Internal gravity waves generated by an impulsive plume, *Phys. Rev. Fluids* **4**, 014803 (2019).
- [21] M. M. Scase and S. B. Dalziel, An experimental study of the bulk properties of vortex rings translating through a stratified fluid, *Eur. J. Mech. B Fluids* **25**, 302 (2006).
- [22] M. M. Scase and S. B. Dalziel, Internal wave fields generated by a translating body in a stratified fluid: An experimental comparison, *J. Fluid Mech.* **564**, 305 (2006).
- [23] P. F. Linden, The interaction of a vortex ring with a sharp density interface: A model for turbulent entrainment, *J. Fluid Mech.* **60**, 467 (1973).
- [24] J. Olsthoorn and S. B. Dalziel, Vortex-ring-induced stratified mixing: mixing model, *J. Fluid Mech.* **837**, 129 (2017).
- [25] J. Olsthoorn and S. B. Dalziel, Vortex-ring-induced stratified mixing, *J. Fluid Mech.* **781**, 113 (2015).
- [26] W. J. A. Dahm, C. M. Scheil, and G. Tryggvason, Dynamics of vortex interaction with a density interface, *J. Fluid Mech.* **205**, 1 (1989).
- [27] M. J. Stock, W. J. A. Dahm, and G. Tryggvason, Impact of a vortex ring on a density interface using a regularized inviscid vortex sheet method, *J. Comput. Phys.* **227**, 9021 (2008).
- [28] D. Schanz, A. Schröder, S. Gesemann, D. Michaelis, and B. Wieneke, Shake-The-Box: A highly efficient and accurate tomographic particle tracking velocimetry (TOMO-PTV) method using prediction of particle positions, in *10th International Symposium on Particle Image Velocimetry PIV13* (Delft, The Netherlands, 2013).
- [29] D. Schanz, S. Gesemann, and A. Schröder, Shake-the-box: Lagrangian particle tracking at high particle image densities, *Exp. Fluids* **57**, 70 (2016).
- [30] N. Didden, On the formation of vortex rings: Rolling-up and production of circulation, *JAMP* **30**, 101 (1979).
- [31] M. Gharib, E. Rambod, and K. Shariff, A universal time scale for vortex ring formation, *J. Fluid Mech.* **360**, 121 (1998).
- [32] G. Oster, Density gradients, *SciAm* **213**, 70 (1965).
- [33] D. Schanz, S. Gesemann, A. Schröder, B. Wieneke, and M. Novara, Non-uniform optical transfer functions in particle imaging: Calibration and application to tomographic reconstruction, *Meas. Sci. Technol.* **24**, 024009 (2013).

- [34] B. Wieneke, Volume self-calibration for 3D particle image velocimetry, *Expt. Fluids* **45**, 549 (2008).
- [35] B. Lüthi, A. Tsinober, and W. Kinzelbach, Lagrangian measurement of vorticity dynamics in turbulent flow, *J. Fluid Mech.* **528**, 87 (2005).
- [36] G. A. Rosi and D. E. Rival, A Lagrangian perspective towards studying entrainment, *Expt. Fluids* **59**, 19 (2018).
- [37] P. Orlandi, P. Egermann, and E. J. Hopfinger, Vortex rings descending in a stratified fluid, *Phys. Fluids* **10**, 2819 (1998).
- [38] S. Voropayev, Modeling of vortex structures in shear flow using a jet of variable impulse, *Morskoy Hydrof. Zh.* **2**, 33 (1987).
- [39] S. Voropayev, Y. Afanasyev, and I. Filipov, Horizontal jets and vortex dipoles in a stratified fluid, *J. Fluid Mech.* **227**, 543 (1991).
- [40] J. B. Flor and G. J. F. Van Heijst, An experimental study of dipolar vortex structures in a stratified fluid, *J. Fluid Mech.* **279**, 101 (1994).
- [41] J. B. Flor, G. J. F. Van Heijst, and R. Delfos, Decay of dipolar vortex structures in a stratified fluid, *Phys. Fluids* **7**, 374 (1995).
- [42] R. Godoy-Diana, J.-M. Chomaz, and P. Billant, Vertical length scale selection for pancake vortices in strongly stratified viscous fluids, *J. Fluid Mech.* **504**, 229 (2004).